ADVANCED FUNCTIONAL MATERIALS
www.afm-journal.de

Self-Assembly Construction of Biomass Aerogel with Tip-To-Based Gradient Porous Structure to Break Trade-Off Effect for Efficient Water/Oil Separation

Zirong Liang, Chen Liang, Wanhe Li, Zuqiang Huang, Huayu Hu, Tao Gan, and Yanjuan Zhang**

Self-driven water/oil separation is an effective and sustainable strategy for oil dehydration, and regulating the pore structure of separation materials to break the trade-off effect between flux and retention remains a challenge. Inspired by the tip-to-base conduit widening structure of vascular bundle, an enthalpy–entropy co-driven strategy based on tannin/amylose non-covalent self-assembly and borate ester dynamic crosslinking is innovatively proposed for constructing a gradient porous biomass aerogel (termed as Si@TAP-B), realizing synchronous improvement of separation flux and retention rate. The permeation fluxes of water/oil mixture and water-in-oil emulsion by Si@TAP-B achieve 17914.7 and 10285.6 L m^{-2} h^{-1}, respectively, and the retention rates remain above 99%. The asymmetric solvent transport induced by gradient porous structure optimizes the hydraulic resistance and breaks the trade-off effect of separation flux and retention. Therefore, the emulsion separation flux under forward osmosis (from large pores to small pores) is twice that under reverse osmosis. Additionally, similar to the self-healing ability of plants, Si@TAP-B can restore the original structure and function after severe damage through reversible crosslinking of borate ester bonds and the flow of low surface energy materials. Overall, this novel strategy is desirable for developing biodegradable, efficient, and durable separation materials with unique structures and functions.

1. Introduction

Oil is an essential resource for promoting the development of modern industry. During processing, transportation, and storage, the moisture content in oil inevitably increases, leading to polarity and oxidation of the oil.[1–3] In addition, the deterioration of oil quality and the presence of fuel oil additives can promote the formation of emulsified oil, thereby affecting the appearance, quality, and performance of the oil products. Even a tiny amount of moisture in the oil can increase the use risk. For instance, 0.1% of emulsified water in the oil will condense on the metal surface of the engine to induce corrosion.[4] Traditional separation techniques can effectively remove immiscible water/oil mixtures, but efficient separation of emulsified oils (droplet size < 20 μm) remains a challenge.[5] 2D membranes, with the advantages of low energy consumption and high efficiency, have been applied to separate various industrial emulsions. However, the 2D membrane structure with low porosity and short permeation channels usually causes serious pollution and degradation because of the adsorption of surfactants and the blockage of pores, leading to a rapid decline in the separation performance.[6–11] Furthermore, the usage of nonbiodegradable petroleum-based materials can generate serious secondary pollution. Alternatively, 3D biomass aerogels have been regarded as promising separation materials because of the interconnected hierarchical network structure, low density, and high internal surface area.[12–15] The aerogels have been mainly used as adsorbents for oil/water separation in previous studies.[16–23] Owing to the 3D interconnected microporous and mesoporous networks of aerogel, oil weighing tens to hundreds of times higher than its own weight can be easily retained in it by capillary forces. Such a structure is generally not conducive to the penetration of oil phase, and the use of aerogels as filter membranes is rarely reported. So far, several strategies have been developed to overcome this shortcoming. Typically, regulating the pore structure (such as anisotropy, directional vertical alignment, hierarchical pores, etc.) of biomass aerogels can reduce the mass transfer resistance of solvent and provide high throughput in oil/water separation.[24–27] However, previous efforts still exist the trade-off effect between separation flux and retention rate in the complex emulsion systems. In addition, the inherent mechanical stability and hydrophilicity of biomass materials limit the application performance of biomass aerogels in water/oil emulsion separation.

Z. Liang, C. Liang, W. Li, Z. Huang, H. Hu, T. Gan, Y. Zhang
School of Chemistry and Chemical Engineering
Guangxi University
Nanning 530004, China
E-mail: huangzq@gxu.edu.cn; zhangyj@gxu.edu.cn
Z. Huang, H. Hu, T. Gan, Y. Zhang
Key Laboratory of New Low-carbon Green Chemical Technology
Education Department of Guangxi Zhuang Autonomous Region
Nanning 530004, China

The ORCID identification number(s) for the author(s) of this article can be found under https://doi.org/10.1002/adfm.202424873

DOI: 10.1002/adfm.202424873

Therefore, manipulating the hierarchical structure of biomass aerogels becomes a critical issue for applying them as efficient filtration membranes.

Woody plants possess nearly perfect vascular bundles with a tip-to-based conduit widening structure to transport water and nutrients, which is an adaptation favored by natural selection. The widening structure helps to minimize the increase in hydraulic resistance, which would otherwise occur as the growth of individual stems and the increase of conductive path length.[28–30] The gradient structure of vascular bundles provides a successful sample for balancing flux and retention of porous materials. In addition, the compositions of vascular bundles mainly include cellulose, hemicellulose, and lignin, which act as supporting skeleton, matrix material, and reinforcement, respectively.[31–33] Therefore, plants exhibit excellent stability and impact resistance in complex real-world environments, demonstrating extraordinary tissue repair capabilities even after severe trauma caused by non-biological or biological environmental stimuli.[34] Therefore, we intend to integrate self-healing functions into separation material, aiming to achieve enhanced durability and service life during the long-term water/oil separation processes.

Starch, a biodegradable and cost-effective polysaccharides, is commonly applied for the preparation of biomass aerogels. Nevertheless, the starch-based aerogels are usually fragile due to rigid macromolecular chains and abundant hydrogen bonds.[35,36] To promote the mechanical performance of starch-based aerogels, biocompatible and biodegradable polyvinyl alcohol (PVA), a good candidate in constructing strong and tough materials via forming reversible borate ester bonds with borax, was employed to composite with starch.[37–39] However, the rapid crosslinking of PVA and borax leads to strong short-range interaction to form dense gel structure, which hinders the diffusion and uniform distribution of ions.[40–42] When the capillary force caused by drying occurs, this interaction will make the gel network shrink or even collapse, thereby increasing the density and reducing the porosity of aerogels. Tannin (TA), rich in phenolic hydroxyl and carbonyl groups, has been widely used as a coagulant to change the physicochemical properties of starch via the non-covalent interaction between TA and amylose (AM).[43–45] Similar to the interaction of polyphenols with proteins, TA and AM are multi-stage spontaneous reactions co-driven by enthalpy–entropy. TA can not only form intermolecular hydrogen bond, but also coordinate with hydrophobic interaction along the α-1,4-glucoside bond of AM through the CH—π bond, forming insoluble nanoparticles.[46] Compared with amylopectin (AP), AM with linear glucose molecular structure and smaller steric hindrance is easier to react with TA. The hydrophobicity of starch can be improved by TA/AM no-covalent interaction. TA/AM complex has been applied as the main component of emulsifiers, and the emulsion with different particle sizes can be achieved by regulating the mass ratio of TA/AM.[47,48] In addition, the self-assembly combination of TA and polysaccharide is beneficial for improving the self-supporting property of polysaccharide-based aerogel, so as to avoid the collapse of pore structure due to the strong short-range interaction between macromolecular chains caused by the capillary force during drying.[49] Although TA/AM composites have been widely studied, the pore regulation and pore formation mechanisms applied to aerogels have not been deeply investigated.

How to effectively regulate the pore structure of biomass-based 3D porous separation materials to break the trade-off effect between flux and retention is an intractable challenge. Inspired by the tip-to-based conduit widening structure of vascular bundle, an enthalpy–entropy co-driven strategy was innovatively created to fabricate a unique 3D gradient porous and self-healing biomass-based aerogel (termed as TAP-B aerogel) via TA/AM non-covalent self-assembly and borate ester dynamic covalent bond crosslinking. The TAP-B aerogel was hydrophobically modified via polydimethylsiloxane/octadecylamine (PDMS/ODA) impregnation to prepare a superhydrophobic self-healing Si@TAP-B aerogel. For the Si@TAP-B aerogel, the insoluble TA/AM nanocomplexes (TA/AM NPs) serve as the "cellulose" hard skeleton, and the TA/AP complexes serve as the "hemicellulose" soft matrix, which are packed against each other, while polyvinyl alcohol (PVA) functions as "lignin" to play a consolidating and supporting role. Graded concentration polymerization of TA/AM NPs induced ice crystal growth to form gradient porous biomass aerogels, which brings two advantages: 1) with gradient distribution of highly porous biomass aerogels along the axial direction, Si@TAP-B promotes internal coalescence and demulsification of the emulsion through pore-throat effect; 2) asymmetric solvent transport (AST) "from large pores to small pores" synchronously improves the flux and retention of water/oil separation. In addition, the synergistic effect of borate ester dynamic covalent bond crosslinking and self-healing hydrophobic coating enables Si@TAP-B aerogel to have a self-healing function similar to that of plant tissue damage. To the best of our knowledge, this work is the first to report the preparation of self-healing biomass aerogels with gradient porous structure using the TA/AM enthalpy–entropy co-driven strategy. The application of asymmetric solvent transport mechanism for water/oil separation may provide a new idea to design high-throughput filtered biomass aerogels, and show great potential to replace traditional non-degradable polymer membranes.

2. Results and Discussion

2.1. Design of Gradient Porous Si@TAP-B Aerogel

Based on the excellent gel-forming capacity and outstanding biodegradable performance of PVA, self-healing gradient porous TAP-B aerogel was synthesized by virtue of the self-assembly property between maize starch (MS) and TA, as well as the reversible crosslinking between borax and 1,2- or 1,3 diols. **Figure 1** schematically demonstrates the preparation of the gradient porous Si@TAP-B aerogel by a concentration-gradient TA/AM NPs settlement approach. In brief, MS and PVA were mixed in water to form a hydrogel, and then a certain concentration of TA and borax solution was added into the MS/PVA mixture in sequence to initiate molecular assembly and borate ester bonds crosslinking. The interaction between AM and TA through the hydrophobic non-covalent interaction, including the intermolecular hydrogen bond and the CH—π bond of the starch pyranose ring and the aromatic residues of phenolic substances. The irreversible enthalpy–entropy co-driven self-assembly reaction promoted the formation of TA/AM NPs. Then, the asymmetric distribution of TA/AM NPs is caused by gravitational sedimentation. TA/AM NPs gathering at the bottom induced ice

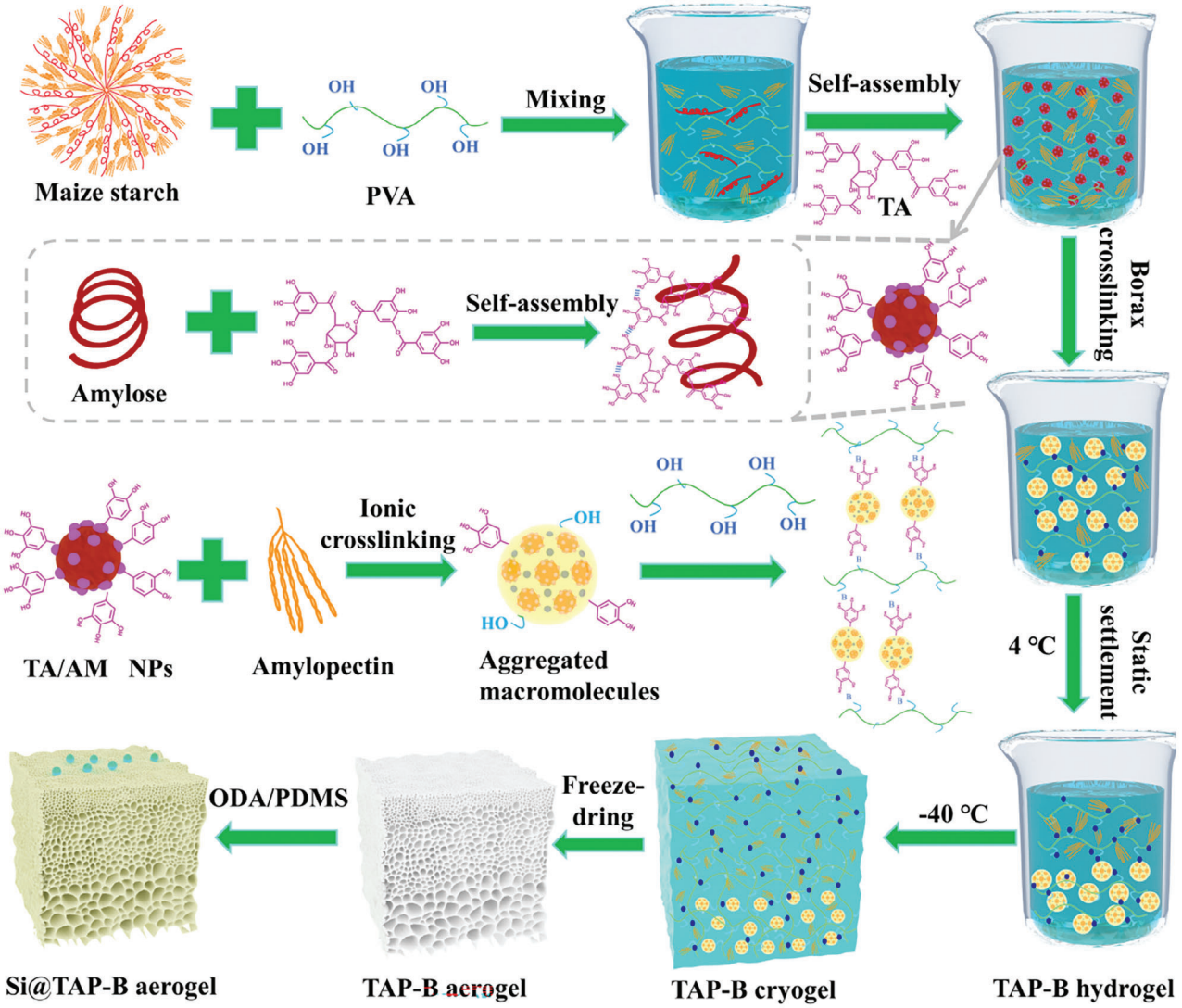

Figure 1. TA/AM enthalpy–entropy co-driven self-assembly strategy to construct gradient porous Si@TAP-B aerogel under ambient conditions.

crystal growth to form a macroporous skeleton. Specifically, the insoluble TA/AM NPs act as a "cellulose" supporting skeleton, which is integrated with the TA/AP complexes that act as a "hemicellulose" matrix binder, while PVA-B acts as a "lignin" reinforcement to withstand capillary force caused by drying. The hydrogel was further converted into a gradient porous biomass aerogel (TAP-B) via a straightforward freeze-drying process. To enhance its hydrophobicity and durability in complex and humid conditions, TAP-B was silanized using PDMS/ODA via direct liquid-phase impregnation to construct the Si@TAP-B aerogel with self-healing superhydrophobicity. For comparison, the samples with different TA/AM mass ratios were prepared by adjusting the TA content under the same conditions. The distribution ratios of each group are shown in Table S1 (Supporting Information).

Figure 2A illustrates the difference in macro morphology of various aerogels. For comparison, the aerogels were prepared in the same mold with a diameter of 2.4 cm through a lyophilization process. In the highly interconnected gel networks, the growth of ice crystals cannot uniformly introduce pores and cohesive cell wall structures in the precursor suspensions. Therefore, the freeze-dried aerogels obtained from the dense gel structure of MP-B short-range interaction collapsed during the thawing–drying stages, forming a foam with volume shrinkage. Figure 2B shows that two flower petals can steadily shore up the TAP-B aerogel, demonstrating its low density. Furthermore, the TAP-B aerogel (0.2 g; 43.0 mg cm^{-3}) can support a weight of 500 g with ≈9% compressive deformation (Figure 2C), demonstrating the favorable compressive strength. In contrast, the TA/MS-B and MS-B aerogels without PVA collapsed immediately under a load of 500 g.

2.2. Structure Evolution of Si@TAP-B Aerogel

In this study, the Si@TAP-B aerogel with gradient porous structure was synthesized by the co-driven strategy via regulating the non-covalent self-assembly of TA/AM and the borate ester

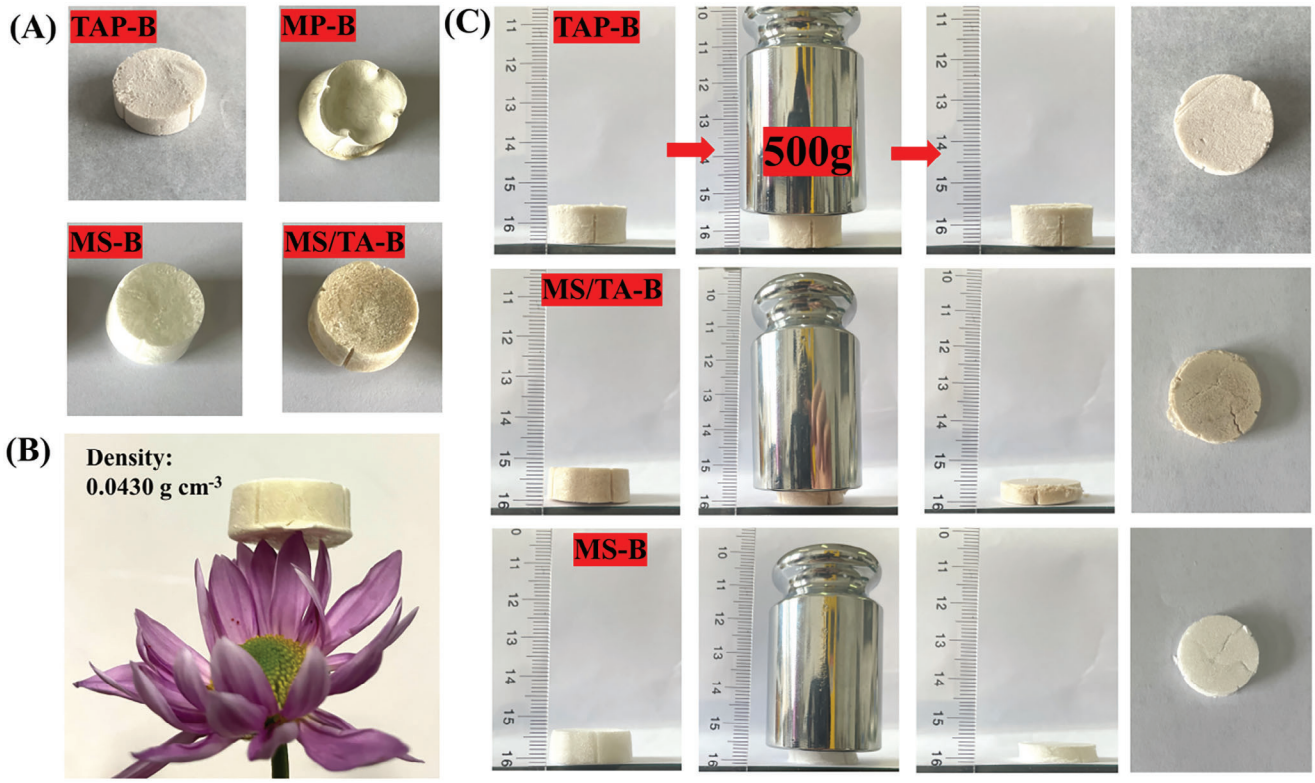

Figure 2. A) Macro morphology of various aerogels. B) TAP-B aerogel (43.0 mg cm^{-3}) stands on the top of flower petals. C) Each aerogel withstands 3000 times its weight and shows recoverability after loading and unloading.

dynamic covalent bond crosslinking. Therefore, the interaction between components was investigated for inferring the formation of gradient pores in Si@TAP-B.

The FTIR spectra of MS, TA, PVA, TAP-B, and MP-B are depicted in **Figure** 3A. The spectrum of TA shows a series characteristic peaks at 1701, 1619, 1533, and 1444 cm^{-1}, which belong to C═O bond, C═C bond in the benzene ring, C—H bond, and the stretching vibration of the phenolic C—OH bond, respectively. In addition, the wide characteristic peak at 3200–3500 cm^{-1} is attributed to the combined effect of the stretching vibration of hydroxyl groups and the intramolecular hydrogen bonding.[50] The spectrum of MS also shows a wide characteristic peak at 3460 cm^{-1}, which is attributed to the stretching vibration of hydroxyl groups. Compared with TA and MS, no new characteristic peak appears in the spectrum of TAP-B complex, only the shift of partial absorption peaks of TA or MS, indicating no covalent interaction between them. The non-covalent interaction between the chemical groups of different compounds can cause the shift of the absorption peak. After the formation of TA/AM complex, the two characteristic peaks of TA at 1701 and 1619 cm^{-1} moved to 1742 and 1660 cm^{-1}, respectively. The movement of functional groups indicates that TA and MS formed hydrogen bonding interaction. In addition, the C–H stretching vibration peak at 2920 cm^{-1} (MS) and the C═C stretching vibration peak of aromatic ring at 1619 cm^{-1} (TA) moved to 2948 and 1660 cm^{-1} (TAP-B complex), respectively, ascribed to the inclusion of TAP-B complex formed by hydrophobic interaction between TA and MS.[46] Additionally, the characteristic absorption peak of boron ester bonds presents at 1353 cm^{-1}. X-ray photoelectron spectroscopy (XPS) survey spectrum (Figure 3B) shows the existence of C, O, and B in TAP-B. The O 1s spectrum of TAP-B (Figure S1A, Supporting Information) shows a characteristic peak at 535.1 eV, corresponding to the B—O—C bond. Furthermore, the B 1s spectrum of TAP-B (Figure S1B, Supporting Information) was fitted to two peaks at 191.3 eV (B—OH) and 189.9 eV (B—O—C), confirming the formation of dynamic borate ester bonds in TAP-B.[51]

The interaction between TA and MS in the PVA-B system was studied by UV–vis (Figure 3C). The UV–vis spectra of TAP-B and TA/AM-B shows a blueshift in the characteristic peak of TA (from 275 to 260 nm). Comparing PVA and TA solutions, the peaks in the UV–vis spectra of TA-B and TA/PVA-B systems remain basically unchanged (Figures S2 and S3, Supporting Information). Besides, TA/AM-B and TAP-B suspensions show higher nonspecific absorbance compared to TA/PVA-B and TA-B. Therefore, TA displays a much higher binding capacity with MS, which is primarily driven by secondary interactions (hydrogen bonding, van der Waals forces, and CH—π interactions). TA exists in the system in different configurations, one is bound to MS by noncovalent interaction, and the other is free molecules.[52]

The thermal stability of the complexes was further investigated by TG analysis (Figure 3D,E). Compared with TA, the initial decomposition temperature of TAP-B and MP-B complexes increased, indicating that the thermal stability of the complexes is higher than that of TA, especially the pyrolysis temperature of TAP-B is the highest. In addition, the initial decomposition temperature of TAP-B complex is lower than that of MS, indicating

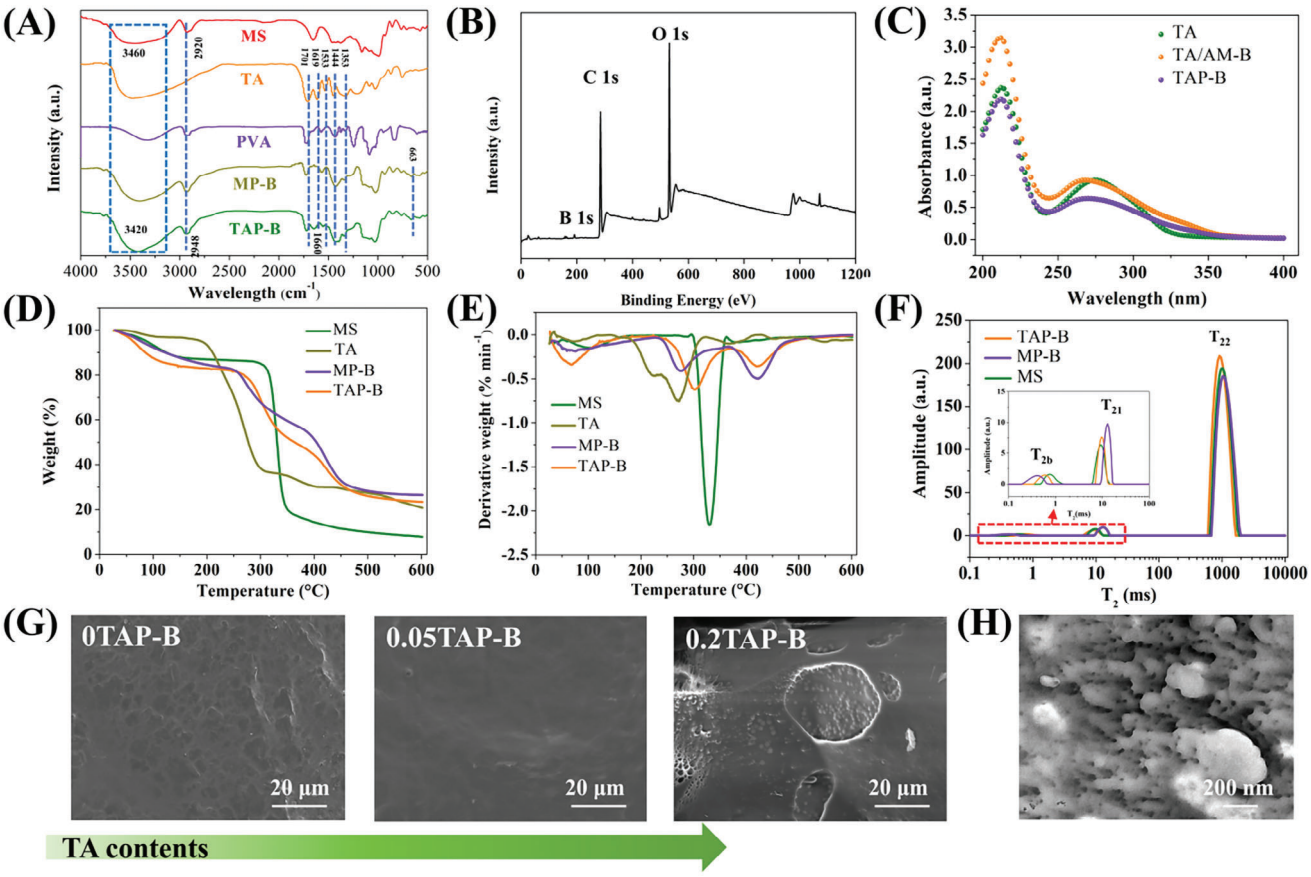

Figure 3. Structure characterization and morphology observation. A) FTIR spectra of MS, TA, PVA, MP-B, and TAP-B. B) XPS spectrum of TAP-B. C) UV–vis spectra of TA, TA/MS-B, and TAP-B. D) TG and E) DTG curves of MS, TA, MP-B, and TAP-B. F) Transverse relaxation time of water distribution in MS, MP-B, and TAP-B. G) SEM images of TAP-B with different TA/MS mass ratios (0–0.2). H) TEM image of 0.2TAP-B.

that the structure of MS in the complex was changed, and the thermal stability of TAP-B complex was reduced compared with MS. The decomposition peak of TA exists at 270 °C, and the peak temperature is lower than that of MS and TAP-B, indicating the strong interaction between TA and MS. A new material phase was formed in the TA/MS complex, and the interaction changed the thermal stability of TA and MS.[53] In addition, Figure 3E presents that the TAP-B and MP-B complexes containing PVA exhibit two pyrolysis peaks, with the C–C cracking peak of MS near 300 °C and the C—C cracking peak of PVA near 422 °C, while the C—C cracking peak of MS in the former is higher. This reveals that TA plays a role as a "bridge" in the system to improve the compatibility of MS and PVA, and it is also due to the strong interaction between TA and AM.

The water distribution in different states is related to the formation of ice crystals. Usually, the polyhydroxyl structure of polysaccharide and PVA can inhibit the growth of ice crystals, owing to that the hydrogen bonds between polysaccharide and water molecules form more bound water. As the vapor pressure of bound water is much lower than that of free water, the bound water is not easy to freeze at the same temperature.[54] The lateral relaxation time was measured by low field NMR (LF-NMR) to analyze the water distribution in TAP-B, MP-B, and MS hydrogel and the interaction between them (Figure 3F; Table S2, Supporting Information). T_{2b}, T_{21}, and T_{22} represent the transverse relaxation times of different states of water in the hydrogel. T_{2b} is the relaxation time of binding water, ranging from 0.1 to 100 ms; T_{21} is the relaxation time of the unflowing water contained in the gel structure, ranging from 10 to 100 ms; T_{22} is the relaxation time of free water, ranging from 100 to 1000 ms.[55] The longer the T_{22}, the freer the water, and the weaker the interaction between hydrogel and water molecules. The proportion of water in different states can be judged by the peak area of water separation in different groups (A_{2b}, A_{21}, and A_{22}).[56] The results indicate that the proportion of free water in the hydrogel samples is high, and the signal amplitude of T_{22} is dominant, with the largest peak value. The signal amplitude of T_{21} is relatively small, while the signal amplitude of T_{2b} is only a small part. Compared with raw MS, the T_{2b} of MP-B decreases, while T_{21} increases, and the proportion areas of A_{2b} and A_{21} increase significantly. The dynamic borate ester bonds crosslinking causes part of free water bound in the 3D network structure of MP-B, and the T_{2b} and T_{21} of TAP-B are higher than those of MP-B, with the decrease in the proportion of bound water (A_{2b} and A_{21}). The increase in the proportion of free water indicates that the introduction of TA weakened the bonding between hydrogel and water molecules, and the non-covalent self-assembly reaction of TA and AM replaced part of the hydrogen bonds, reducing the bound water in the system.

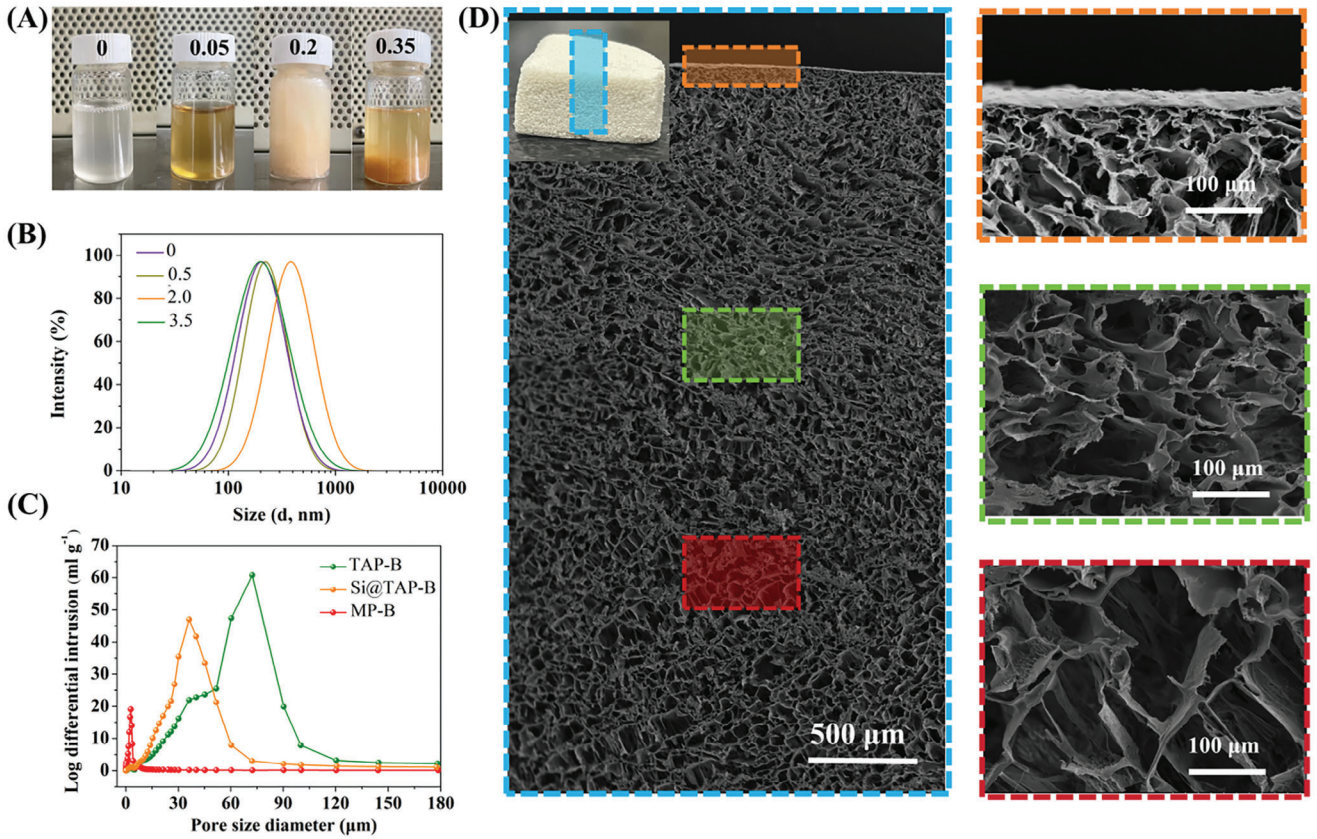

Figure 4. A) Optical image of TAP-B emulsion gel with different TA contents. B) Droplet size distribution of TA/AM NPs with different TA contents. C) Macroscopic pore size distribution obtained by mercury-intrusion porosimetry. D) SEM images of 0.2TAP-B aerogel at full vertical section.

The insoluble TA/AM NPs play a crucial role in determining the porous structure of Si@TAP-B. As shown in Figure 3G, no obvious agglomeration of TA/AM NPs is observed in 0TAP-B and 0.05TAP-B. However, more particles are observed in 0.2TAP-B, revealing that excess TA led to serious agglomeration. The pore walls of TAP-B are filed with agglomerated TA/AM NPs. Further evidence obtained by high-resolution transmission electron microscopy (TEM) substantiates that TA/AM NPs presented nanoscale dispersion in the TAP-B matrix with the dispersion size <200 nm (Figure 3H), which facilitates the formation of nanophase interfaces and the growth of ice crystals, thus forming rich pore structure in the aerogel.

The gradient pore structure of Si@TAP-B was caused by the asymmetric concentration distribution of TA/AM NPs. As shown in **Figure** 4A, the color of the TAP-B emulsion changes from colorless to milky white, eventually forming a precipitate and undergoing phase separation as the increase of TA content. Figure 4B shows the droplet size distribution and average size of TAP-B with different TA contents. When the TA/AM mass ratio is 0.2, the droplet size is the largest, but excessive TA caused a large amount of precipitation, resulting in a decrease in droplet size. This reveals the self-assembly and self-emulsification property between TA and MS, which is consistent with the three-step spontaneous in situ complexation of TA and MS reported by Wei et al.[46] During the in-situ polymerization, the TA/AM NPs colloidal particles undergo nucleation and secondary growth processes. In the nucleation stage, a tiny amount of TA and AM mainly form soluble complex; with the increase of TA content, further association occurs to form small insoluble complex with the soluble ligand as the nucleation center. Subsequently, the generated insoluble TA/AM NPs separate from the solution and form individual particles. At last, more TA can combine on the surface soluble/insoluble complexes and act as a linking agent, resulting in the formation of large aggregates even precipitates with the increase of TA content. During the secondary growth stage, small dispersed particles gradually merge into large particles, and the TA/AM NPs with different sizes aggregate to form a gradient concentration distribution and eventually a connected gradient porous structure.

The microstructure of TAP-B aerogel was evaluated using cross-section observation (Figure 4D). The cutaway section of TAP-B aerogel exhibits obvious gradient pores widening along the axial and interconnecting to form a vascular bundle-like porous structure. Local magnification reveals a noticeable trend of increasing pore size from top to bottom, which is consistent with the gradient concentration distribution of TA/AM NPs. Besides, the 0TAP-B aerogel without TA exhibits dense continuous stacked layers and sparse micropores, and the top surface is smooth and flat (Figure S4A, Supporting Information), which is due to the lack of TA/AM NPs as a skeleton support and the strong short-range interaction caused by the rapid crosslinking of PVA with borax. Therefore, the capillary force caused by

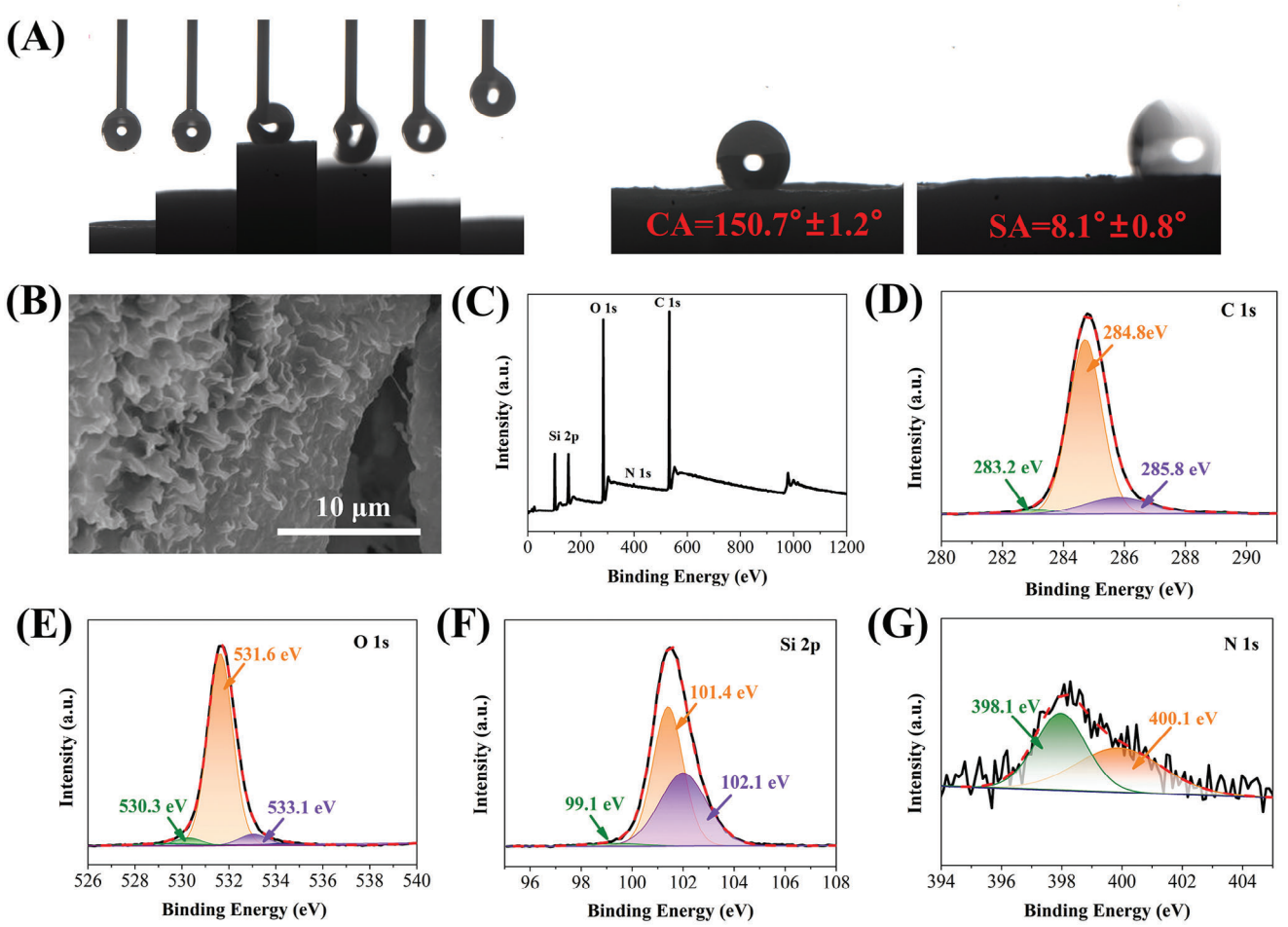

Figure 5. A) Wettability of the superhydrophobic Si@TAP-B aerogel. B) Surface morphology of Si@TAP-B. C–G) Surface chemical composition of Si@TAP-B.

drying can induce severe structural shrinkage inside 0TAP-B. According to the measurement of pore structure and the observation of field emission scanning electron microscopy (FE-SEM), it can be concluded that the presence of TA can induce the growth of ice crystals to form rich pore structure in aerogel. Moreover, due to a large number of polar hydrophilic functional groups distributing on the surface of biomass aerogel, it is easy to shrink as the capillary force caused by drying, so there are great limitations in selecting hydrophobic modification methods, which can be observed from the SEM images of Si@TAP-B at low magnification (Figure S4C, Supporting Information). The surface and cross-section of Si@TAP-B still retain a small and dense pore structure. Mercury-intrusion porosimetry test (Figure 4C) demonstrates that the porosity of the aerogel was still maintained at 92.26% after silicification modification, while the pore size decreased from 59.00 to 33.32 μm (Table S3, Supporting Information). TAP-B was subjected to hydrophobic modification by impregnation, and the pore structure was optimized on the basis of retaining the original characteristics.

Dynamic water adhesion measurement was performed to evaluate the hydrophobicity of Si@TAP-B aerogel (**Figure** 5A). When a water droplet (4 μL) was brought into full contact with the surface of Si@TAP-B and then lifted underwater, no traces of water was observed on the aerogel. Additionally, the self-cleaning function of Si@TAP-B was evaluated by the sliding angle (SA) test. Briefly, water drops were added to the superhydrophobic surface of Si@TAP-B in advance, and the tilt angle of the sample platform was set in the program until the water drops slipped. The tilt angle of the recorder is the SA of the test sample. For Si@TAP-B, the water contact angle (WCA) is 150.7° ± 1.2° and the SA is only 8.1° ± 0.8°. High-power observation of the Si@TAP-B surface indicates that PDMS/ODA formed a mountain-shaped coating structure on the surface of TAP-B (Figure 5B). The enhanced surface roughness combined with the modification of low surface energy endow the 3D porous aerogel with superhydrophobicity. Meanwhile, Si@TAP-B exhibited satisfactory stability, even under acidic and alkaline conditions, with WCA exceeding 140° (Figure S5, Supporting Information).

XPS test was conducted to further analyze the surface chemical composition of Si@TAP-B (Figure 5C–G). The full spectrum scan confirms the presence of C, N, O, and Si elements. There are three distinct peaks at 283.2, 284.8, and 285.8 eV in the C 1s spectrum, corresponding to the C—Si, C—C, and C—N bonds, respectively. The C—Si and C—N bonds originate from PDMS

and ODA, respectively. In the O 1s spectrum, three peaks at 530.3, 531.6, and 533.1 eV are assigned to the C—OH, C═O, and Si—O—Si bonds, respectively.[57] The existence of Si—O—Si bond also proves the existence of PDMS, with other bonds consisting in the framework of TAP-B aerogel. The two peaks at 398.1 and 400.1 eV in the N 1s spectrum correspond to the C—N and —NH_2 bonds, respectively. In the Si 2p spectrum, three peaks presenting at 99.1, 101.4, and 102.1 eV correspond to the bond energies of C—Si, O—Si—O, and Si—O—Si, respectively, originating from the surface modified ODA. The XPS analysis proves that PDMS/ODA is successfully coated on the surface of TAP-B aerogel.

2.3. Self-Healing Behavior of Superhydrophobic Si@TAP-B Aerogel

Inspired by the self-healing ability of plant vascular bundles that enables the materials to exhibit a long service life, high durability, and environmental friendliness, in this study, the self-healing properties of Si@TAP-B were investigated from two perspectives: mechanical damage self-healing and chemical erosion self-healing. As shown in **Figure 6**A, Si@TAP-B was first cut into half with a razor blade. The cross interfaces were moistened with deionized water (pH 7) and then contacted mutually for geometrical matching. After full contact at 25 °C for 2 h, the halves can be assembled into a single unit that can support its own weight. According to wettability test, the water droplets attached to its cross section cannot achieve self-cleaning performance, and its WCA drops to 134°. After contacted at 70 °C for 1 h, the water droplets can roll off the surface, and WCA reaches 151°, indicating that the sample has completed self-healing ability with superhydrophobic performance. To further investigate the self-healing performance of Si@TAP-B, an optical microscope was used for observation. As shown in Figure 6B, there is a distinct groove in the contact region when they contact at room temperature only, which disappears after being thermally-driven at 70 °C. This region was further studied by SEM (Figure 6C). Highly coarse clusters appear at the section, the same as in the undamaged area, indicating that the hydrophobic structure has been recovered. The self-healing mechanical properties of Si@TAP-B were evaluated by tensile test.

Since all molecular chains are fixed in the dry state, when the super-hydrophobic aerogel is cut off, it cannot be self-healing. It is necessary to wet the section with solution first, and change the aerogel at the section position into the hydrogel, which makes the molecular chains move freely. To further explore the self-healing mechanism of Si@TAP-B matrix, five aqueous solutions, $NaIO_4$, urea, HCl (pH 1), H_2O (pH 7), and NaOH (pH 11), were used to wet the cross-sections for self-healing measurements (Figures S6 and S7, Supporting Information). The tensile forces of the self-healing Si@TAP-B were 0, 1.58, 0.81, 1.95, and 2.02 MPa, and the corresponding healing efficiencies were 0, 67%, 35%, 81.6%, and 85.1%, respectively. The results indicate that the tensile force and healing efficiency of Si@TAP-B improve with the increase in the pH of aqueous solution, which is directly related to the dynamic crosslinking of boron ester bonds in the wet section. When the pH value of the wetting solution is low, the hydroxyl groups are protonated and the boron ester bonds are broken. On the contrary, when the wetting solution is in an alkaline state (pH > 9), the hydrogen bonds between molecules gradually dissociate, and the hydroxyl and borate groups recombine to form coordination covalent bonds. As a result, the higher the pH value of the wetting solution, the stronger the boron ester bond crosslinking on both sides of the Si@TAP-B cross-section. Meanwhile, a large number of hydroxyl groups on both sides of the cross-section can form hydrogen bonding, which is beneficial for self-healing. Through wetting the cross-section with urea solution, hydrogen bonds could be shielded. Compared with the tensile force in the presence of hydrogen bonding, the healing efficiency of Si@TAP-B after wetting with urea solution only decreased by 14.6%. Therefore, it can be inferred that the dynamic crosslinking of boron ester bonds is the main driving force for Si@TAP-B. Furthermore, the Si@TAP-B aerogel lost self-healing function after wetting the cut surface with $NaIO_4$ solution, and the tensile force decreased to 0. $NaIO_4$ can oxidize the catechol groups on the cut surface to quinone-like or quinone groups, and the quinone groups cannot cross link with borax. As shown in Figure 6D, compared with Si@TAP-B, Si@MP-B exhibited a higher tensile stress (4.36 MPa), and after repair, and its tensile strength only recovered to 2.13 MPa, with a mechanical healing efficiency of 42%. The strong short-range interaction between diols and borax in the system can form a tightly cross-linked structure that makes it difficult for the wetting solution to enter, leading to the molecular chains between the cross-sections unable to move freely. Here, TA active molecules with rich catechol groups serve as a key mediator in the system and can be programmed to perform a variety of dynamic interactions with other components, such as borate ester bonds and hydrogen bonds, capable of reversibly breaking and rebuilding.

In addition, superhydrophobic filter materials still suffer from serious pollution in the practical application of water/oil separation, which makes the surface energy higher. Plasma etching technology was used to change the surface energy of materials to accelerate the process of interface pollution. As shown in Figure 6G, Si@TAP-B can rapidly improve its surface energy and decrease its WCA to 29° after being etched by O_2 plasma for 1 min. After being heated at 50 °C for 20 min, its WCA returns to 151°. Even after 12 etching/healing cycles, WCA can still reach 147°, showing strong resistance to chemical erosion. To further investigate the self-healing mechanism of Si@TAP-B, XPS was used to analyze the chemical composition changes of its superhydrophobic surface after an etching/healing cycle. The XPS survey spectra (Figure S8A, Supporting Information) indicate that the etching and healing processes led to significant changes in the proportion of elements on the surface of Si@TAP-B. According to the high-resolution C 1s and O 1s spectra of Si@TAP-B (Figure S8B,C, Supporting Information), the element ratio of Si@TAP-B before/after healing was calculated (Table S4, Supporting Information). The O/C ratio of original Si@TAP-B is 0.27, which rapidly increases to 1.4 after being etched by O_2 plasma, while decreases to 1.19 after self-healing. The characteristic peak of the C═O groups increases while that of the C—C groups decreases after self-healing, indicating that the oxygen-containing functional groups with high surface energy cover the hydrophobic alkyl chains, and the surface of the aerogel becomes hydrophilic. In contrast, the hydrophobic alkyl chains on the surface of the healing aerogel increase, while the hydrophilic

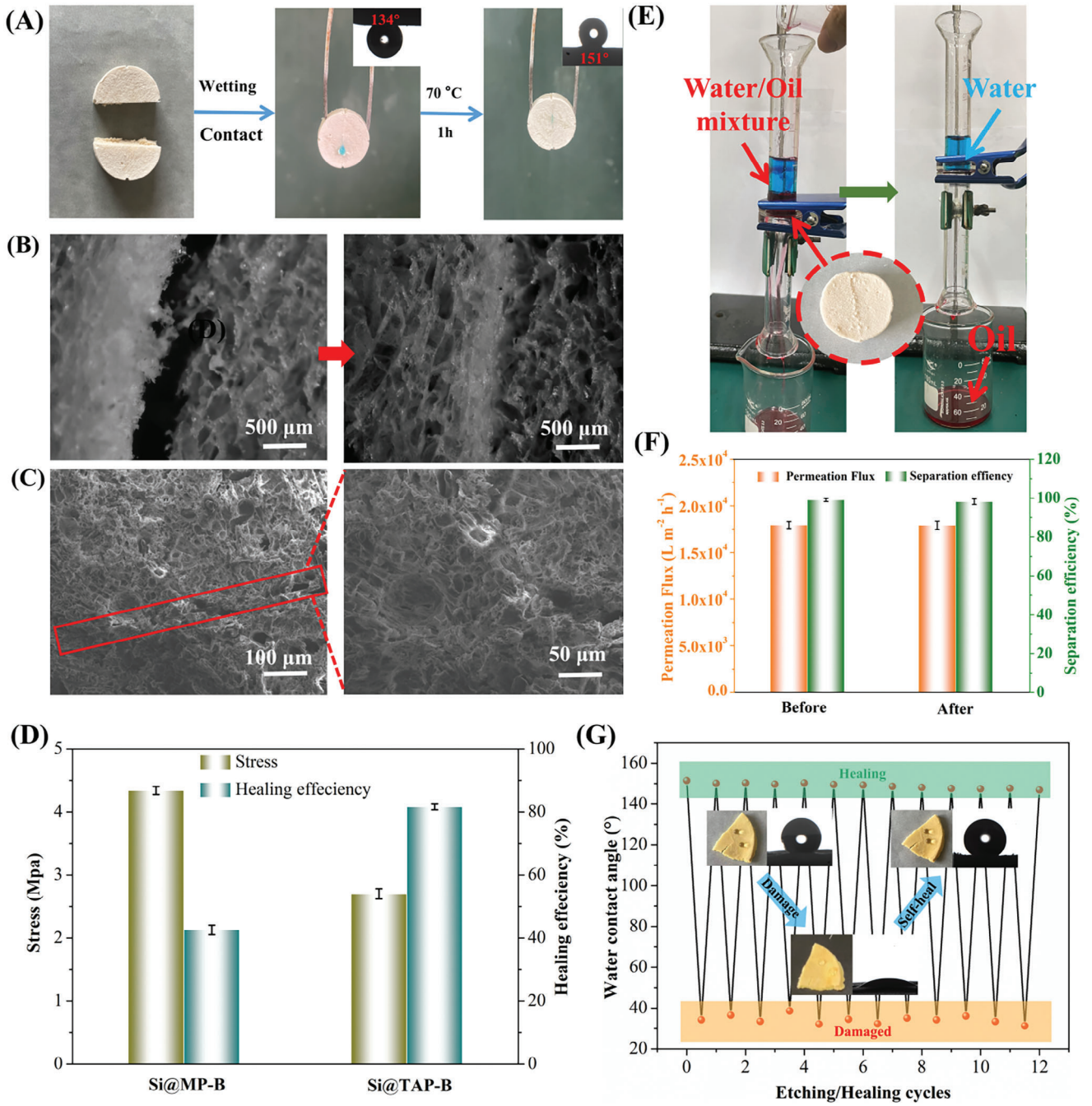

Figure 6. A) Photographs showing the cutting and self-healing of Si@TAP-B. B) Optical microscopy images of the contact region before (left) and after (right) heating. C) SEM image of the healed region. D) Healing efficiency parameters of Si@MP-B and Si@TAP-B aerogels. E) Water/oil separation using self-healing Si@TAP-B aerogel. F) Comparison of flux and separation efficiency of original and self-healing Si@TAP-B aerogel. G) Variation of WCA during repeated etching/healing cycles.

oxygen-containing functional groups decrease.[57] With the increase in the surface energy of Si@TAP-B due to chemical erosion, the low surface energy material ODA is melted by thermal drive to cover the high surface energy area with cooling and recrystallization, thus providing a continuous supply of surface energy materials for Si@TAP-B.[58] Combined with the repairable borate ester crosslinked skeleton, it provides the aerogel with strong self-healing properties.

The application superiority of self-healing properties in water/oil separation was evaluated by comparing the separation performance of Si@TAP-B aerogel before damage and after self-healing (the self-healing Si@TAP-B was used as a filter layer, as

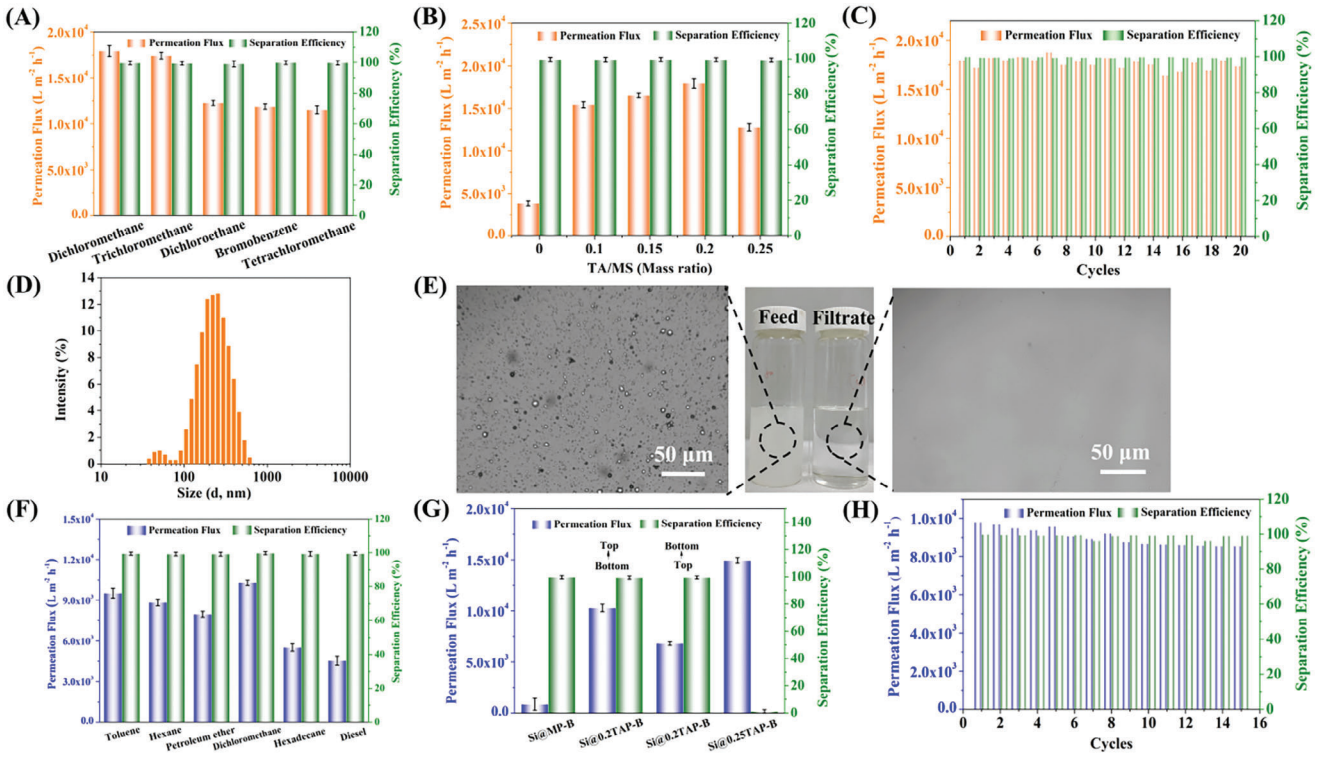

Figure 7. A) Separation performance of Si@TAP-B for various immiscible water/oil mixtures. B) Separation performance of Si@TAP-B with various TA/AM mass ratios for immiscible water/dichloromethane mixture. C) Cyclic separation performance of Si@TAP-B for water/dichloromethane mixture. D) Dynamic light scattering for measuring water size distribution of water-in-toluene emulsion. E) Digital images of Si@TAP-B filter after separating 10 mL of water-in-toluene emulsion. F) Separation performance of Si@TAP-B for various emulsions. G) Separation performance of Si@TAP-B with various TA/AM mass ratios for water-in-toluene emulsion. H) Cyclic separation performance of Si@TAP-B for water-in-toluene emulsion.

shown in Figure 6E). It is found that the structural overlap induced the collapse of pores at the fracture, thus reducing the oil phase flow path and resulting in the loss of separation flux. After fracture repair by self-healing, the separation efficiency of Si@TAP-B was still above 99%, with a flux of 17 913 L m^{-2} h^{-1} (Figure 6F). It can maintain 97.7% of the original performance, showing superior self-healing characteristics.

2.4. Evaluation of Water/Oil Separation Performance

To evaluate the application performance of Si@TAP-B in water/oil separation, two water/oil systems, immiscible water/oil mixture (V_{water}:V_{oil} = 1:1) and water-in-oil emulsion (V_{water}:V_{oil} = 1:99), were chosen for investigation. In the self-designed separation device (Figure S9, Supporting Information), the immiscible water/oil mixture and water-in-oil emulsion were treated with a 5 mm thick Si@TAP-B filter layer. When an immiscible water/oil mixture was poured into the device, the oil layer rapidly permeated through the Si@TAP-B aerogel filter, while the water was effectively repelled and retained in the upper funnel. Other immiscible water/oil (dichloromethane, chloroform, tetrachloromethane, dichloroethane, or bromobenzene) mixtures were similarly separated to obtain the corresponding separation efficiency (E_{ff}) and oil flux values (**Figure** 7A). The fluxes of Si@TAP-B for various water/oil mixtures are 17 945.7, 17 422.6, 12 258.1, 11 865.3, and 11 523.8 L m^{-2} h^{-1}, respectively, and the E_{ff} of all immiscible water/oil mixtures are >99.9%. It indicates that the separation process was almost complete without additional driving pressure. Since the TA/AM NPs play a key role in constructing porous structure, the Si@TAP-B aerogels with various TA/AM mass ratios were used for separating immiscible water/dichloromethane mixture (Figure 7B). Although the E_{ff} of all samples achieved 99%, the Si@TAP-B aerogel without TA exhibited a low oil flux for water/dichloromethane mixture which required at least 6 min to separate 20 mL of water/dichloromethane mixture (Movie S1, Supporting Information). For the Si@TAP-B aerogels containing TA, the flux for separating water/dichloromethane mixture was high, which required only 20 s to separate 20 mL of water/dichloromethane mixture (Movie S2, Supporting Information). Furthermore, increasing the mass ratio of TA/AM in the aerogel significantly enhanced the separation flux of water/oil mixture from 3824.5 L m^{-2} h^{-1} (without TA) to 17 914.7 L m^{-2} h^{-1} (with TA/AM mass ratio of 0.2). This phenomenon is due to that the irreversible self-assembly reaction between the TA and AM molecules weakens the internally strong borate ester bonds crosslinking structure of Si@MP-B, and the TA/AM complex acts as self-supporting skeleton to promote the porosity from 55% to 96%, providing abundant permeation paths.[58] However, excessive TA causes the rise in crosslinking density of the polymer and the reduction in separation flux. Another important feature of the successful design of water/oil separation materials is reusability. As shown in Figure 7C, the Si@TAP-B aerogel exhibited stable performance

for separating water/dichloromethane mixture after 20 cycles, ascribed to its strong mechanical durability and chemical stability.

Different from immiscible water/oil mixture, the surfactant-stabilized water-in-oil emulsion tends to form small water droplets with high stability and complex structure, which is still a rigorous challenge for 3D biomass aerogels due to the trade-off effect between permeability and selectivity. In this study, Tween-80 (0.1 wt.%) was used as the surfactant to prepare a series of surfactant-stabilized water-in-oil emulsions, including light oils (represented by dichloromethane, hexane, petroleum ether, and toluene) and heavy oils (represented by hexadecane and diesel). Optical microscopic images of the emulsions were measured, and the distribution of water droplets was tested by DLS (Figure 7D,E; Figure S10, Supporting Information). As shown in Figure 7F, all the surfactant-stabilized water-in-oil emulsions were successfully separated by Si@TAP-B filtration under gravity driving condition. For the water-in-toluene emulsion with the average water droplet size of 12.18 μm, the oil permeation flux was 9521.8 L m^{-2} h^{-1} with the water rejection of 99.34%, and the whole process was only 29 s (Movie S3, Supporting Information). The optical microscopic images indicate that compared with the emulsion before filtration, the resulting filtrate changed from the original milky white to clear and transparent, without the existence of small water droplets, confirming the successful separation of the emulsion. The separation performance of Si@TAP-B for water-in-dichloromethane, water-in-hexane, and water-in-petroleum ether emulsions was assessed by same method. Similarly, all of them could be effectively separated with ultrahigh oil flux (from 7970.8 to 10 285.6 L m^{-2} h^{-1}). However, compared to the light oil emulsions, the heavy oil emulsions is relatively difficult to be separated, with the separation fluxes of only 5523 and 4543 L m^{-2} h^{-1} for the water-in-hexadecane and water-in-diesel emulsions, respectively. Different emulsions have different molecular structures and molecular polarities, resulting in different binding energies with water molecules and therefore different separation difficulties. It can be noted that the separation flux of Si@TAP-B is higher than that of the reported water/oil separation materials (Table S5, Supporting Information). In addition, separation performance stability tests were performed to evaluate the durability of Si@TAP-B. As shown in Figure 7H, for 15 cycles of separation tests, the separation efficiency all maintained above 99.9%, and the separation flux was still as high as 8533.7 L m^{-2} h^{-1}, corroborating outstanding structural stability and reusability.

The separation performance of Si@TAP-B under a vacuum degree of 0.04 MPa for 5 consecutive cycles (12 min per cycle) was also investigated with water-in-hexane emulsion as the separation sample (Figure S11, Supporting Information). In the first cycle, the original separation flux of Si@TAP-B was 1.92×10^5 L m^{-2} h^{-1} MPa^{-1}, with the stable flux of 1.41×10^5 L m^{-2} h^{-1} MPa^{-1} and the retention rate of 99.9%. After 5 cycles, the separation flux of Si@TAP-B decreased by 33.8% over time and could not be recovered by washing with alcohol, but the separation efficiency still reached 98.7%. Furthermore, the biodegradation of the aerogels was measured by buried in the soil (Figure S12, Supporting Information). The degradation rate of the reference sample reached 72.01% after 45 days of burial, indicating the effectiveness of the biodegradation experiment. The degradation rate of TAP-B reached 58.08% after 45 days of burial, with a great shrinkage and the loss of its original appearance. Compared to the aerogel without hydrophobic modification, water and fungi are less likely to enter the interior of Si@TAP-B. However, from a morphological perspective, the Si@TAP-B surface was covered by the yellow fungi. After 45 days of biodegradation, weight loss, and morphological defects continued to occur, with a biodegradation rate of 49.86%. This reveals that the Si@TAP-B aerogel can be degraded by soil microorganisms, avoiding secondary pollution to the environment. Evidently, the Si@TAP-B aerogel exhibits excellent water/oil separation performance as well as self-healing and biodegradable functions, which are superior to the water/oil separation materials reported in recent years (Table S5, Supporting Information).

Resolving the trade-off effect of flux and retention remains a great challenge, whereas 3D porous polymer can overcome the size mismatch between pore size and emulsion droplets by regulating pore size and relying on interconnected porous networks. In this study, the Si@TAP-B aerogels with different pore sizes, prepared with different TA/AM mass ratios, were used as 3D separation filter layers to prove that the gradient porous separation materials can effectively solve the trade-off effect in emulsion separation. As shown in Figure 7G, Si@TAP-B with a small aperture (Si@MP-B) exhibited a separation efficiency of >99%, but its separation flux was low, which required at least 10 min to separate 20 mL of water-in-toluene emulsion (Movie S4, Supporting Information), due to the poor permeability and over-emphasis on selectivity. On the contrary, Si@TAP-B with a large aperture (Si@0.25TAP-B) exhibited a higher separation flux, but its selectivity was poor. The Si@0.2TAP-B aerogel with gradient porous structure can realize the effective separation of emulsion. It is noteworthy that Si@0.2TAP-B exhibits asymmetric solvent transport when different sides of the separation material were used as the feed end during the filtration process. The separation flux at the feed end of the "large to small" aperture direction is 37.2% higher than that at the reverse feed end, which is similar to the result reported by Zuo et al.[59] According to the Bernoulli differential equation and the Venturi effect,[60] fluid velocity can be accelerated when a fluid passes through a shrinking flow channel, and vice versa. Alternatively, according to the plant hydraulic wide tube model proposed by Loren et al.,[61] the hydraulic resistance of pipes with pore diameter varying along the length (i.e., graded vascular bundle structure of plants) can be minimized while the risk of embolization and carbon cost are minimized. In extreme cases, infinitely graded porous structures can result in infinite fluid velocities. To better explain the occurrence of this phenomenon, the mechanism of emulsion separation enhanced by the gradient porous structure of Si@TAP-B was further investigated by Computational Fluid Dynamics (CFD).[62]

2.5. Enhanced Demulsification Performance of Si@TAP-B and Inherent Mechanism

3D porous materials have complex interconnected pore structures, and there is still a lack of effective characterization methods to trace the internal fluid flow, so the water/oil separation mechanism is usually speculated. In this study, the water/oil separation process was simulated by CFD to study the flow process of fluid in the Si@TAP-B aerogel and reveal its separation mechanism. The

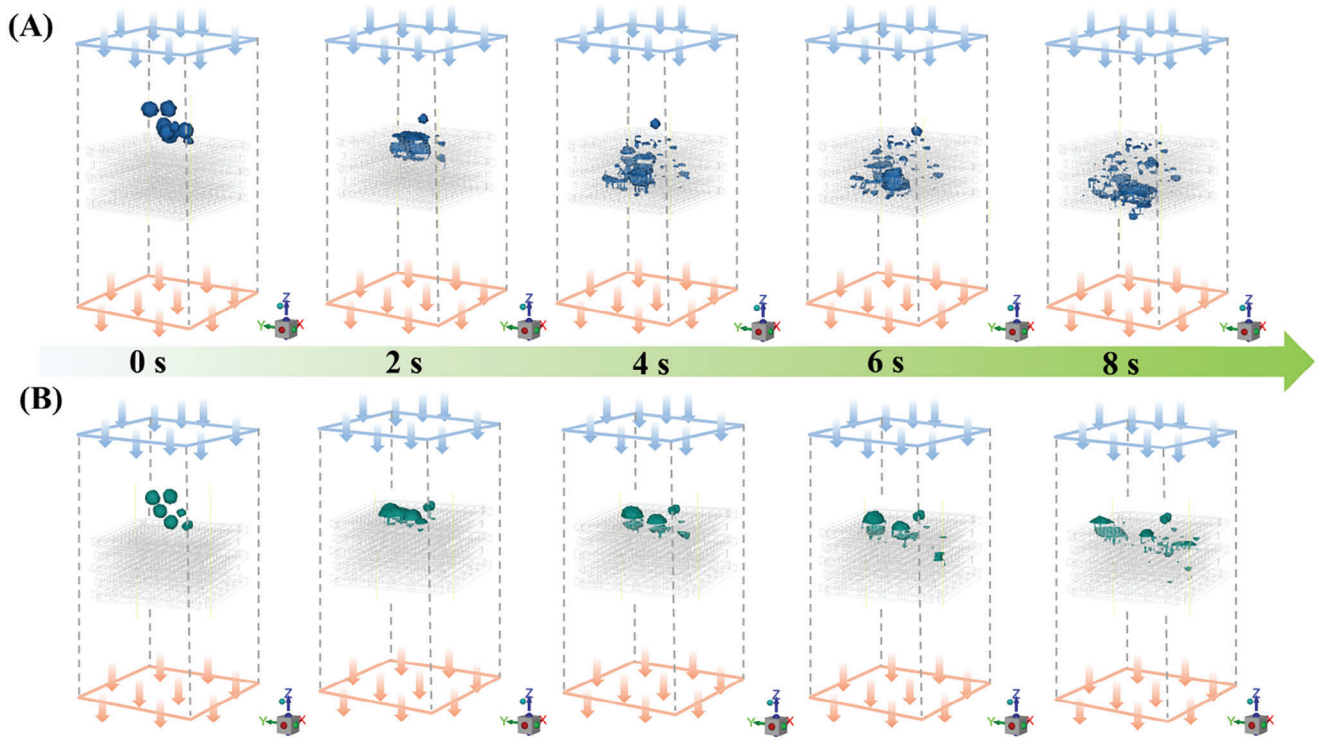

Figure 8. Simulation model of water/oil emulsion separation by Si@TAP-B. Flow trajectory of the water droplets in different directions during the separation process: A) Forward flow (from large pores to small pores); B) Reverse flow (from small pores to large pores).

results of SEM analysis and mercury injection test demonstrate that Si@TAP-B has a gradient porous structure widening along the axial direction. Five separate layers with different pore sizes were made to construct the geometric model, with a gradual transition from the top pore size of 60 μm to the bottom pore size of 10 μm (Figure S13A, Supporting Information). Then, according to the actual conditions of emulsion separation, the corresponding model was established (Figure S13B, Supporting Information), in which oil was a transparent continuous phase and water was a dispersed phase. The specific parameters were set according to the actual situation (Table S6, Supporting Information). The simulation model was then meshed to form a grid model (Figures S13C and S14, Supporting Information). The orthogonality mass of the mesh is >0.2, which allows accurate calculation of the emulsion separation results. Finally, the boundaries were defined: the upper boundary is the pressure inlet; the lower boundary is the mass outlet; all other boundaries are the walls; the initial velocity is zero; the initial pressure is zero; the gravity is 9.8 m s^{-1}.

To observe the flow of water droplets in oil in the Si@TAP-B aerogel, the flow path of water droplets (the blue/green spheres represent water droplets) along the top side as the feed end through the entire filter layer was simulated (the oil phase is set to transparent). In the forward flow (**Figure** 8A), due to the large hole with a diameter of 60 μm at the top, all liquid droplets can smoothly pass through the surface layer and enter the Si@TAP-B interior. With the decrease of the aperture, during the falling process of water droplets, the collision probability of various water droplets greatly increases. Due to the extrusion effect and interface repulsion with low surface energy at the throat of the hole, the interface between the emulsions is unstable and deformed. Finally, the water droplets fuse together to form large droplets, which can be successfully intercepted. On the contrary, in the reverse flow (Figure 8B), water droplets in the emulsion tend to aggregate on the surface to form a hydration layer, resulting in a "cake effect" similar to the 2D membranes, leading to a decrease in separation flux. The unique internal aggregation and interception mechanism formed by squeezing coalescence demulsification can effectively avoid the disadvantage of water droplets gathering on the surface of the filter layer to form a hydration layer in the traditional separation materials, resulting in reduced separation flux.

Figure 9A presents the flow trajectory of the oil phase in the forward flow, in which the oil phase successfully passes through the entire filter layer in a V-shape during the filtration simulation. In the reverse flow (Figure 9B), the small surface aperture of the mobile phase causes excessive surface intrusion pressure, resulting in backflow phenomenon. After the same time step, most of the mobile phase in reverse flow is still trapped in it. The asymmetric solvent transport phenomenon in the gradient porous structure of Si@TAP-B was further analyzed by establishing a plane in each layer of the model and conducting numerical calculation of the average velocity and pressure of the plane (Figure S15, Supporting Information). The forward flow speed increases with the increase of the number of layers, and the pressure decreases with the increase of the number of layers. In the reverse flow of the feed end, the changes of velocity and pressure are exactly the opposite. The velocity vector cloud and pressure cloud

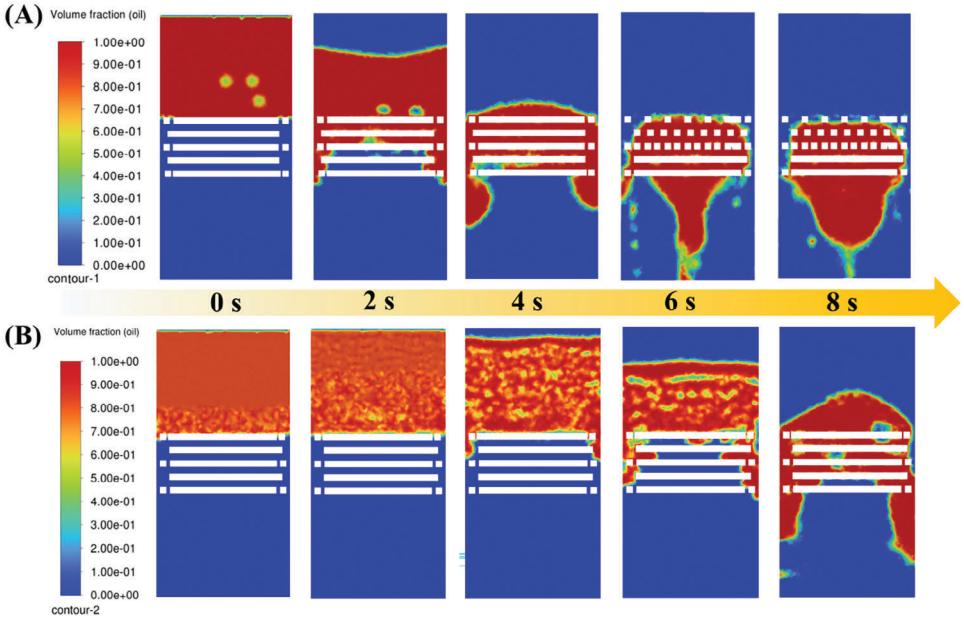

Figure 9. Iso-surfaces of the oil volume fraction (value = 0.9) for monitoring the behavior of the separated oil. A) Forward flow; B) Reverse flow.

images (Figures S16 and S17, Supporting Information) provide an intuitive perspective. When the fluid flows through a porous filter layer with gradient widening, the graded number of gradient pores can lead to a higher multiple of flux difference. In theory, the forward fluid flow is higher than the reverse fluid flow. According to the Venturi or Bernoulli equation, as the fluid moves from a large aperture to a small aperture, the flow velocity increases and the pressure decreases. The thickness of the pipeline is equivalent to a fluid velocity filter, and those with a large axial velocity component are likely to quickly pass through the thin tube. On the contrary, those with a larger radial velocity component have a lower probability of passing through the thin tube, while those with slower fluid velocity have a stronger pressure (static pressure) on the thick tube wall at a macroscopic level, and those with faster velocity have a lower pressure on the thin tube wall. In extreme cases, the infinite gradient porous structure may lead to infinite fluid velocity or non-flowing systems with forward and reverse fluxes, revealing the underlying reasons for the different permeation fluxes of Si@TAP-B in different feed directions.

The emulsion separation process in the Si@TAP-B aerogel is visualized by CFD simulation. Its gradient porous structure makes the droplets have more chances to collide through the extrusion effect of pore throat, which destroys the stability of the double electric layer of emulsifier and accelerates demulsification, resulting in the water droplets to gather into large droplets that are readily intercepted inside. This unique internal interception phenomenon can effectively prevent water droplets from forming a hydration layer on the surface of the feed end in the separation material, thereby rapidly reducing the separation flux. In addition, the Venturi effect generated by the gradient porous structure of Si@TAP-B optimizes the flow resistance due to the accumulation of oil phase, resulting in higher separation flux and retention in the feed direction from large holes to small holes. The mechanism analysis based on experiment and simulation verifies that the unique porous structure of Si@TAP-B effectively breaks the trade-off effect in traditional water/oil separation materials.

3. Conclusion

Herein, inspired by the asymmetric solvent transport phenomenon of vascular bundle with tip-to-based conduit widening structure, an enthalpy–entropy co-driven strategy was innovatively proposed to fabricate a unique gradient porous Si@TAP-B biomass aerogel via TA/AM non-covalent self-assembly and borate ester dynamic covalent bond crosslinking. TA/AM NPs acted as "cellulose" to form the main supporting skeleton and TA/AP acted as "hemicellulose" filling between the components to provide adhesion, while PVA acted as "lignin" to provide strength and defense. The reversible dynamic crosslinking of borate ester bonds and the heat-sensitive hydrophobic coating of PDMS/ODA contributed to excellent self-healability of Si@TAP-B. The Si@TAP-B aerogel was used for separating various immiscible water/oil mixtures and Tween-80-stabilized water-in-oil emulsions under gravity, which exhibited stable and high permeation fluxes up to 17 945.7 and 10 285.6 L m^{-2} h^{-1}, respectively, with a relatively high separation efficiency of 99% over 15 cycles. Additionally, the emulsion separation process model was numerically simulated by CFD to reveal the inherent separation mechanism of the gradient porous Si@TAP-B, especially the effective breaking of the trade-off effect between flux and retention. Overall, this work indicates that the Si@TAP-B biomass aerogel has great potential in complex water/oil separation due to the advantages of biodegradability, excellent self-healing and self-cleaning ability, and high permeation flux and separation efficiency.

Supporting Information

Supporting Information is available from the Wiley Online Library or from the author.

Acknowledgements

This research was supported by the National Natural Science Foundation of China (Nos. 22068007 and 22268005).

Conflict of Interest

The authors declare no conflict of interest.

Author Contributions

Z.H. conceived the project and designed experiments. Z.L. conducted the experiments and characterizations with the help of C.L., W.L., and T.G. Z.L. and Y.Z. wrote the manuscript. H.H. and Y.Z. supervised the experiments and characterizations. Z.L. filmed the Supplemental Video. All authors discussed the results and commented on the manuscript.

Data Availability Statement

The data that support the findings of this study are available from the corresponding author upon reasonable request.

Keywords

oil dehydration, self-healing aerogel, trade-off effect, vascular bundle structure

Received: December 16, 2024
Published online:

[1] X. Zeng, L. Qian, X. Yuan, C. Zhou, Z. Li, J. Cheng, S. Xu, S. Wang, P. Pi, X. Wen, *ACS Nano* **2017**, *11*, 760.
[2] E. C. Zuleta, L. Baena, L. A. Rios, J. A. Calderón, *J. Brazil. Chem. Soc.* **2012**, *23*, 2159.
[3] M. Wu, S. Huang, C. Liu, J. Wu, S. Agarwal, A. Greiner, Z. Xu, *J. Mater. Chem. A.* **2020**, *8*, 11354.
[4] M. A. Fazal, A. S. M. A. Haseeb, H. H. Masjuki, *Fuel Process. Technol.* **2010**, *91*, 1308.
[5] J. S. Eow, M. Ghadiri, *Chem. Eng. J.* **2002**, *85*, 357.
[6] J. Ge, J. Zhang, F. Wang, Z. Li, J. Yu, B. Ding, *J. Mater. Chem. A.* **2017**, *5*, 497.
[7] X. Tan, C. Hu, X. Li, H. Liu, J. Qu, *J. Membr. Sci.* **2020**, *605*, 118088.
[8] Y. Liu, Y. Su, J. Guan, J. Cao, R. Zhang, M. He, Z. Jiang, *ACS Appl. Mater. Interfaces* **2018**, *10*, 26546.
[9] E. Tummons, Q. Han, H. J. Tanudjaja, C. A. Hejase, J. W. Chew, V. V. Tarabara, *Sep. Purif. Technol.* **2020**, *248*, 116919.
[10] G. Liu, Y. Cai, H. Yuan, J. Zhang, Z. Zhang, D. Zhao, *J. Membr. Sci.* **2023**, *668*, 121077.
[11] G. Gu, X. Yang, Y. Li, J. Guo, J. Huang, E. N. Nxumalo, B. B. Mamba, L. Shao, *Separat. Purific. Technol.* **2025**, *356*, 129848.
[12] S. Yang, L. Chen, S. Liu, W. Hou, J. Zhu, P. Zhao, Q. Zhang, *J. Hazard. Mater.* **2021**, *408*, 124408.
[13] F. Wang, R. Ma, Y. Tian, *Int. J. Biol. Macromol.* **2022**, *207*, 549.
[14] Q. Shang, J. Cheng, L. Hu, C. Bo, X. Yang, Y. Hu, C. Liu, Y. Zhou, *Colloids Surf., A* **2022**, *636*, 128043.
[15] G. Jiang, J. Ge, Y. Jia, X. Ye, L. Jin, J. Zhang, Z. Zhao, G. Yang, L. Xue, S. Xie, *Sep. Purif. Technol.* **2021**, *270*, 118740.
[16] N. Tian, S. Wu, G. Han, Y. Zhang, Q. Li, T. Dong, *J. Hazard. Mater.* **2022**, *424*, 127393.
[17] Y. Zhang, M. Yin, L. Li, B. Fan, Y. Liu, R. Li, X. Ren, T. Huang, I. S. Kim, *Carbohydr. Polym.* **2020**, *243*, 116461.
[18] S. Fan, Z. Li, C. Fan, J. Chen, H. Huang, G. Chen, S. Liu, H. Zhou, R. Liu, Z. Feng, Y. Zhang, H. Hu, Z. Huang, Y. Qin, J. Liang, *J. Hazard. Mater.* **2022**, *433*, 128808.
[19] F. Ciuffarin, M. Négrier, S. Plazzotta, M. Libralato, S. Calligaris, T. Budtova, L. Manzocco, *Food Hydrocolloid* **2023**, *140*, 108631.
[20] X. Ma, S. Zhou, J. Li, F. Xie, H. Yang, C. Wang, B. D. Fahlman, W. Li, *J. Hazard. Mater.* **2023**, *454*, 131397.
[21] R. Ye, J. Long, D. Peng, Y. Wang, G. Zhang, G. Xiao, Y. Zheng, T. Xiao, Y. Wen, J. Li, H. Li, *J. Hazard. Mater.* **2022**, *438*, 129529.
[22] M. Ren, X. Ji, F. Kong, C. Zhou, A. E. A. Yagoub, J. Liang, X. P. Ye, Z. Gu, Q. Ma, X. Fan, H. Li, *Chem. Eng. J.* **2023**, *475*, 146425.
[23] H. Subhan, S. Alam, L. A. Shah, N. S. Khattak, I. Zekker, *J. Water Process Eng.* **2022**, *46*, 102546.
[24] Y. Yang, Z. Ren, C. Zhou, Y. Lin, L. Hou, L. Shi, S. Zhong, *Adv. Funct. Mater.* **2023**, *33*, 2212262.
[25] T. Dong, H. Ye, W. Wang, Y. Zhang, G. Han, F. Peng, C. Lou, S. Chi, Y. Liu, C. Liu, J. Lin, *J. Hazard. Mater.* **2023**, *454*, 131474.
[26] J. Ge, Q. Jin, D. Zong, J. Yu, B. Ding, *ACS Appl. Mater. Interfaces* **2018**, *10*, 16183.
[27] K. Wang, X. Liu, Y. Tan, W. Zhang, S. Zhang, J. Li, *Chem. Eng. J.* **2019**, *371*, 769.
[28] L. Loepfe, J. Martinez-Vilalta, J. Piñol, M. Mencuccini, *J. Theor. Biol.* **2007**, *247*, 788.
[29] L. Koçillari, M. E. Olson, S. Suweis, R. P. Rocha, A. Lovison, F. Cardin, T. E. Dawson, A. Echeverría, A. Fajardo, S. Lechthaler, C. Martínez-Pérez, C. R. Marcati, K. Chung, J. A. Rosell, A. Segovia-Rivas, C. B. Williams, E. Petrone-Mendoza, A. Rinaldo, T. Anfodillo, J. R. Banavar, A. Maritan, *Proc. Natl. Acad. Sci. U. S. A.* **2021**, *118*, 1.
[30] M. E. Olson, T. Anfodillo, S. M. Gleason, K. A. McCulloh, *New Phytol* **2021**, *229*, 1877.
[31] K. Jin, Z. Qin, M. J. Buehler, *J. Mech. Behav. Biomed. Mater.* **2015**, *42*, 198.
[32] P. Cheng, S. Chen, X. Li, Y. Xu, F. Xu, A. J. Ragauskas, *Energy Convers. Manage.* **2022**, *255*, 115321.
[33] W. Shen, C. Zhang, G. Wang, Y. Li, X. Zhang, Y. Cui, Z. Hu, S. Shen, X. Xu, Y. Cao, X. Li, J. Wen, J. Lin, *Int. J. Biol. Macromol.* **2024**, *268*, 131619.
[34] P. Marhava, L. Hoermayer, S. Yoshida, P. Marhavý, E. Benková, J. Friml, *Cell* **2019**, *177*, 957 .
[35] Q. Zheng, Y. Tian, F. Ye, Y. Zhou, G. Zhao, *Trends Food Sci. Technol.* **2020**, *99*, 608.
[36] F. Zhu, *Trends Food Sci. Technol.* **2019**, *89*, 1.
[37] Y. Qin, J. Wang, C. Qiu, X. Xu, Z. Jin, *J. Agric. Food Chem.* **2019**, *67*, 3966.
[38] J. Hou, M. Liu, H. Zhang, Y. Song, X. Jiang, A. Yu, L. Jiang, B. Su, *J. Mater. Chem. A.* **2017**, *5*, 13138.
[39] J. Li, Y. Deng, H. Fu, Y. Zhang, Y. Zhang, L. Fu, C. Xu, B. Lin, *Small* **2023**, *19*, 2208116.
[40] Z. Bai, K. Jia, C. Liu, L. Wang, G. Lin, Y. Huang, S. Liu, X. Liu, *Adv. Funct. Mater.* **2021**, *31*, 2104701.
[41] Y. Chen, W. Qian, R. Chen, H. Zhang, X. Li, D. Shi, W. Dong, M. Chen, Y. Zhao, *ACS Macro Lett.* **2017**, *6*, 1129.
[42] K. Shang, D. Ye, A. Kang, Y. Wang, W. Liao, S. Xu, Y. Wang, *Polymer* **2017**, *131*, 111.
[43] H. Xie, X. Wei, X. Liu, W. Bai, X. Zeng, *Ultrason. Sonochem.* **2023**, *95*, 106367.
[44] N. Deng, Z. Deng, C. Tang, C. Liu, S. Luo, T. Chen, X. Hu, *Trends Food Sci. Technol.* **2021**, *112*, 667.
[45] T. J. Gutiérrez, J. Tovar, *Trends Food Sci. Technol.* **2021**, *109*, 711.
[46] X. Wei, J. Li, B. Li, *Food Hydrocolloid* **2019**, *94*, 174.
[47] X. Wei, J. Li, M. Eid, B. Li, *Food Hydrocolloid* **2020**, *107*, 105728.

[48] D. Zhang, L. Chen, J. Cai, Q. Dong, Z. Din, Z. Hu, G. Wang, W. Ding, J. He, S. Cheng, *Food Chem.* **2021**, *360*, 129922.
[49] B. D. Mattos, Y. Zhu, B. L. Tardy, M. Beaumont, A. C. R. Ribeiro, A. L. Missio, C. G. Otoni, O. J. Rojas, *Adv. Mater.* **2023**, *35*, 2209685.
[50] X. Sun, P. Jia, H. Zhang, M. Dong, J. Wang, L. Li, T. Bu, X. Wang, L. Wang, Q. Lu, J. Wang, *Adv. Funct. Mater.* **2022**, *32*, 2106572.
[51] Q. Li, S. Zheng, Z. Liu, W. Li, X. Wang, Q. Cao, F. Yan, *Adv. Mater.* **2024**, *36*, 2413901.
[52] B. D. Mattos, Y. Zhu, B. L. Tardy, M. Beaumont, A. Ribeiro, A. L. Missio, C. G. Otoni, O. J. Rojas, *Adv. Mater.* **2023**, *35*, 2209685.
[53] D. Sun, J. Mo, W. Liu, N. Yan, X. Qiu, *Adv. Funct. Mater.* **2024**, *34*, 2403333.
[54] Y. Liu, A. Liu, L. Liu, Z. Kan, W. Wang, *J. Food Process Eng.* **2021**, *44*, e13723.
[55] R. Liu, W. Sun, Y. Zhang, Z. Huang, H. Hu, M. Zhao, *Food Chem.* **2019**, *271*, 284.
[56] T. Kopač, M. Abrami, M. Grassi, A. Ručigaj, M. Krajnc, *Carbohydr. Polym.* **2022**, *277*, 118895.
[57] L. Qin, N. Chen, X. Zhou, Q. Pan, *J. Mater. Chem. A.* **2018**, *6*, 4424.
[58] D. Song, C. Li, J. Li, T. Cao, P. Cai, N. Wang, Q. F. An, *J. Membr. Sci.* **2024**, *696*, 122529.
[59] H. Zuo, B. Lyu, J. Yao, W. Long, Y. Shi, X. Li, H. Hu, A. Thomas, J. Yuan, B. Hou, W. Zhang, Y. Liao, *Adv. Mater.* **2024**, *36*, 2305755.
[60] A. Chandra, D. Pathiwada, S. Chattopadhyay, *Chem. Eng. Res. Des.* **2019**, *142*, 386.
[61] L. Kocillari, M. E. Olson, S. Suweis, R. P. Rocha, A. Lovison, F. Cardin, T. E. Dawson, A. Echeverria, A. Fajardo, S. Lechthaler, C. Martinez-Perez, C. R. Marcati, K. F. Chung, J. A. Rosell, A. Segovia-Rivas, C. B. Williams, E. Petrone-Mendoza, A. Rinaldo, T. Anfodillo, J. R. Banavar, A. Maritan, *Proc. Natl. Acad. Sci. U. S. A.* **2021**, *118*, 2100314118.
[62] Y. Kagawa, T. Ishigami, K. Hayashi, H. Fuse, Y. Mino, H. Matsuyama, *Soft Matter* **2014**, *10*, 7985.